

Monolithic High Contrast Grating Integrated with Metal: Infrared Electrode with Exceptionally High Conductivity and Transmission

Marek Ekielski¹, Weronika Głowadzka², Karolina Bogdanowicz^{1,2}, Michał Rygała³, Monika Mikulicz³, Patrycja Śpiewak², Marcin Kowalski⁴, Marcin Gębski², Marcin Motyka³, Anna Szerling¹, and Tomasz Czyszanowski^{2,*}

¹*Lukasiewicz Research Network - Institute of Microelectronics and Photonics, al. Lotników 32/46, 02-668 Warsaw, Poland*

²*Photonics Group, Institute of Physics, Lodz University of Technology, ul. Wolczanska 219, 90-924 Łódź, Poland*

³*Laboratory for Optical Spectroscopy of Nanostructures, Department of Experimental Physics, Faculty of Fundamental Problems of Technology, Wrocław University of Science and Technology, Wybrzeże Wyspiańskiego 27, 50-370 Wrocław, Poland*

⁴*Institute of Optoelectronics, Military University of Technology, Gen. S. Kaliskiego, 00-908 Warsaw, Poland*
*Corresponding author: tomasz.czyszanowski@p.lodz.pl

August 8, 2023

Abstract

The design of transparent conductive electrodes (TCEs) for optoelectronic devices requires a trade-off between high conductivity or transmittivity, limiting their efficiency. This paper demonstrates a novel approach to fabricating TCEs that effectively alleviates this trade-off: a monolithic GaAs high contrast grating integrated with metal (metalMHCG). The metalMHCG enables higher electrical conductivity than other TCEs, while providing transmissive and antireflective properties. We focus on infrared spectrum TCEs, which are essential for sensing, thermal imaging, and automotive applications. However, due to elevated free carrier absorption they are much more demanding than TCEs for the visible spectrum. We demonstrate 75% absolute transmittance of unpolarized light, resulting in 108% transmittance relative to plain GaAs substrate. We achieved even larger absolute transmittance of polarized light, reaching 92% or 133% relative transmittance. Despite record high transmittance, the sheet resistance of the metalMHCG is several times lower than any other TCE, ranging from 0.5 to 1 ΩSq^{-1} .

Keywords: monolithic high contrast grating; subwavelength grating; transparent conductive electrode

1 Introduction

Optoelectronic technology relies on transparent conductive electrodes (TCEs) enabling electrical conductivity within the electrode plane, current injection to the semiconductor on which the TCE is deposited, and transmittance of light through the TCE. The high concentration of free carriers in TCEs is the main limiting factor affecting the performance of TCEs and imposes a fundamental trade-off between electrical conductivity and light absorption (accompanied by reflection of light propagating through the TCEs, in accor-

dance with the Drude model).

Visible light transparent conductive oxides (TCOs) are widely used as TCEs in liquid crystal displays [1], light-emitting diodes [2], and solar cells [3, 4]. The most common TCO is indium tin oxide (ITO). However, despite its excellent performance, ITO has some significant drawbacks, including high cost, brittleness, recycling difficulties, and the scarcity of indium [5, 6]. To overcome these issues, other TCOs, such as fluorine-doped tin oxide (FTO) and aluminum-doped zinc oxide (AZO), have emerged as attractive alternatives to ITO [7]. Not only do they do not rely on

indium, but they can achieve a high level of absolute transmittance of up to 90%, which is comparable to ITO. Their sheet resistance levels are typically above $10 \Omega \text{Sq}^{-1}$ for transmittance levels of around 80%, which is also similar to ITO.

Other alternatives include ultrathin metals [8–11], conductive polymers [12–14], carbon nanotubes [15, 16], graphene-based layers [17–21], nanowires [22–25], dielectric-metal-dielectric structures [26–31], and metal networks [32, 33]. Of these alternatives, metal nanowires and dielectric-metal-dielectric structures are the most promising, as they exhibit low sheet resistance below $10 \Omega \text{Sq}^{-1}$ and above 90% absolute transmittance. Graphene is also highly attractive, due to its theoretical potential for high conductivity [34] and high transmittance, which can reach 95% for the visible light spectral range in the case of a single graphene monolayer. However, current methods for synthesizing graphene films have resulted in resistance values that are too high for electrodes used in electronic devices [35].

The implementation of TCEs directly on semiconductors is highly desirable for electroluminescent diodes, photodiodes, lasers, and other technologies that predominantly work in the infrared spectral range and where high current density is injected into the devices. The utilization of TCEs in infrared semiconductor devices is impacted by two phenomena that negatively affect their transmittance properties. Firstly, the plasma frequency of free electrons coincides with the frequency of infrared light, which enhances the response of free electrons in the TCEs to electromagnetic excitation. This heightened response leads to increased absorption and reflection, and as a result the transmittivity of infrared TCEs is significantly lower [36–38] compared to TCEs used in the visible range. Recently, S. Wang et al. [21] demonstrated record high infrared light transmittance and low sheet resistance using conductive composite films based on silver nanowires and graphene implemented on a BaF_2 substrate, achieving transmittance over 70% and sheet resistance of $28 \Omega \text{Sq}^{-1}$. However, there is a general lack of research on TCEs in the infrared region, despite their wide range of possible applications in devices for thermal imaging, free space communication, eye-safe LIDARs, and the detection of toxic gases—which in the wavelength range of 4 to $10 \mu\text{m}$ have strong absorption lines.

Secondly, the transmittivity of TCEs implemented on the interface between air and substrate of high refractive index is limited by Fresnel reflection, given by the formula:

$$R = \left(\frac{n - 1}{n + 1} \right)^2 \quad (1)$$

where n is the refractive index of the substrate and the refractive index of air is 1. In the case of glass and polymer substrates, Fresnel reflection is not larger than 5%. The interface between air and most narrow-bandgap semiconductors defined by refractive indices close to 3 introduces reflection of nearly 30%. Thus, if the TCEs discussed earlier are deposited on the surface of a semiconductor, their transmittance will be lower by $\sim 25\%$.

We define the relative transmittance of a TCE as the ratio between the absolute transmittance of the TCE on a transparent substrate and the absolute transmittance of the same substrate without the TCE. This measure allows us to compare the optical properties of TCEs employed for various purposes. Relative transmittance enables determination of the transmittance regardless of the impact of Fresnel reflection. The relative transmittance of the TCEs discussed so far in this article remains below 100%. This is due mostly to the absorption and reflection induced by free carriers. However, it has been demonstrated that by leveraging low quality factor resonance in an $\text{Al}_2\text{O}_3/\text{Cu}/\text{Ag}/\text{ZnO}$ planar configuration, it is possible to achieve a relative transmittance slightly above 100% within the visible light range, while maintaining a sheet resistance of $18 \Omega \text{Sq}^{-1}$ [31].

To address the inherent trade-off between resistivity and transmittivity in TCEs, extend their spectral range of transparency, and mitigate the Fresnel reflection, in [39] we proposed two configurations of semiconductor deep-subwavelength monolithic high-contrast gratings integrated with metal (metalMHCG). The two configurations, named TM and TE, are composed of a one-dimensional semiconductor grating integrated with metal stripes on bulk semiconductor material matching the grating. In the TM configuration metal stripes are implemented on the semiconductor stripes, while in the TE configuration metal stripes are deposited between semiconductor stripes (see Fig. 1). The nomenclature of the configurations is derived from the predominant polarization component of light that is transmitted by them. As such, the TM configuration primarily transmits the TM component of the electromagnetic field, where the electric field of the electromagnetic wave oscillates perpendicular to the stripes in the grating plane (along the y -axis, see Fig. 1). The TE configuration predominantly transmits the TE component, where the electric field oscillates along the grating stripes (along the x -axis, see Fig. 1). In what follows, TE and TM

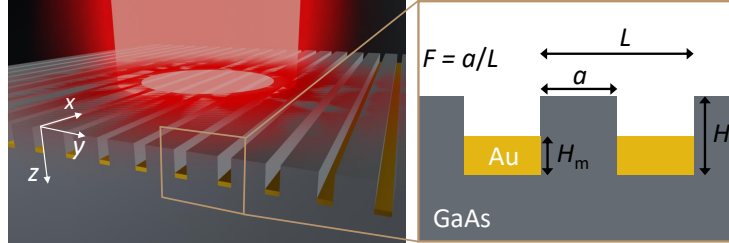


Figure 1: Schematics of the metalMHC configuration composed of one-dimensional grating on a GaAs wafer with gold stripes implemented in the grooves between the semiconductor stripes. The geometrical parameters of the grating and the coordinate system are indicated.

transmittances refer to the transmittances of the TE and TM light components, respectively. Unpolarized light consists of equal TE and TM components. The metalMHC may partially polarize the incident unpolarized light under transmission. However, to characterize the metalMHC in terms of its ability to transfer the energy of unpolarized light regardless of the polarizing effect of the transmission, we define the transmittance of unpolarized light as the average of the TE and TM components that are transmitted, bearing in mind that the transmitted light may be partially polarized.

In [39], we showed by numerical analysis that metalMHCGs in both configurations can achieve absolute transmittance of polarized light of more than 98% (corresponding to a relative transmittance of more than 140%) for electromagnetic radiation ranging from the visible to far infrared spectrum, while their sheet resistance can be less than $1 \Omega \text{Sq}^{-1}$. The high transmittance of the metalMHCG in the visible and infrared ranges is made possible by the low quality factor resonance occurring in the air slits for TM polarization and in the semiconductor stripes of the grating for TE polarization, resulting in reduced light interaction with the metal stripes [40]. Thus, the minimized electron excitation by the electromagnetic wave in metal sustains high transmittance, even when the frequency of light approaches the electron plasma frequency.

In a previous study [43], we experimentally demonstrated 90% transmittance of polarized light through a metalMHCG in the TM configuration with a corresponding sheet resistance of $2 \Omega \text{Sq}^{-1}$. This configuration showed strong discrimination of the orthogonal polarization. According to the numerical analysis, it is evident that the TE configuration, as shown in Fig. 1, exhibits lower polarization discrimination compared

to the TM configuration. In another study [40], we showed by numerical analysis that with an optimised design of the TE configuration absolute unpolarized transmittance as large as 95% can be achieved, corresponding to 137% relative transmittance. However, the optimised configuration for unpolarized light transmittance requires that the height of the semiconductor stripes is twice the period of the grating and the width of the grooves between the stripes is about 20% of the period, which poses a major technological challenge.

Here, we present the experimental realization of a metalMHCG in the TE configuration that is designed to maximize transmittance of TE polarized light in the vicinity of the $9 \mu\text{m}$ wavelength. The metalMHCG achieved 92% absolute transmittance and 133% relative transmittance of TE polarized light compared to a bare GaAs substrate. The transmittance bandwidth of polarized light above 100% of the relative transmittance is wider than $3 \mu\text{m}$. Since in this configuration the metalMHCG also enables high transmittance of the orthogonal light component (TM), the absolute transmittance of non-polarized light reaches 75%. This corresponds to 108% relative transmittance and $2 \mu\text{m}$ bandwidth above 100% of the relative transmittance, even though the metalMHCG is not designed for unpolarized light transmittance as in [40]. Additionally, our metalMHCGs are characterised by sheet resistance of $0.5\text{-}1 \Omega \text{Sq}^{-1}$, which is several times lower than any TCE reported previously. The metalMHCG can be monolithically integrated with a wide range of materials used in optoelectronics, particularly with high refractive index semiconductors, effectively eliminating surface reflection. Additionally, the weak interaction between light and metal in the metalMHCG minimizes metal reflection and absorption. These unique characteristics allow for substantially higher transmittance and metal con-

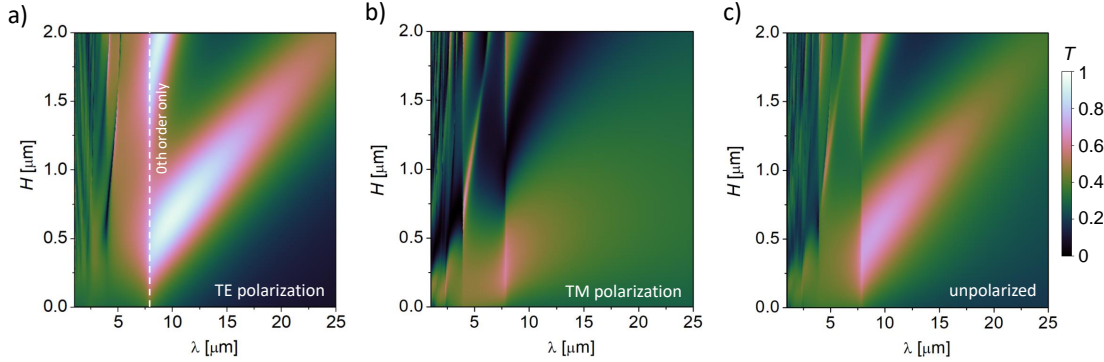


Figure 2: Transmittance (T) maps of metalMHCg under normal incidence of TE polarized a), TM polarized b) and unpolarized light c) in the domain of the wavelength (λ), and height of the semiconductor stripes (H) for $L = 2.4 \mu\text{m}$, $F = 0.7$, $H_m = 0.2 \mu\text{m}$. The white dashed line in a) indicates the limit of the zeroth diffraction order emitted towards substrate. The refractive indices of GaAs and Au are based on values reported in [41, 42]

tent compared to other TCE realizations. As a result, our electrode exhibits low sheet resistance while maintaining high transmittance, even in the challenging infrared electromagnetic spectrum.

2 Results

The metalMHCg in the TE configuration is composed of a monolithic, double-side polished $350 \mu\text{m}$ thick undoped GaAs wafer with parallel stripes etched onto one surface. Gold stripes are deposited in the grooves between the semiconductor stripes (see Fig. 1). The back side of the wafer is not covered with an anti-reflective coating, as most dielectrics have high absorption in the spectral range of interest. The parameters defining the metalMHCg geometry are as follows: L – period of the grating; H , H_m – heights of the semiconductor and metal stripe, respectively; a , a_m – widths of the semiconductor and metal stripe respectively, where $a + a_m = L$; F – the duty cycle, which is the ratio of the width of the semiconductor stripe (a) to the period (L); n_s , n_m – the refractive indices of the semiconductor and metal, respectively. In the numerical analysis that complements the experiment, we assume a semi-infinitely thick wafer and a semi-infinite air superstrate above the grating. We consider a single period of the grating with periodic boundary conditions, which elongates the metalMHCg to infinity in lateral directions. In this section, we will conduct an analysis of absolute and relative transmittances through numerical simulations and experimental measurements. The term “transmittance” will refer to absolute transmittance, whereas relative transmittance will be explicitly indicated.

Numerical design. In this section, we eluci-

date the properties of the optimal metalMHCg structure, before delving into the process of its development. Figure 2 illustrates calculated transmittance maps for close to optimal metalMHCg in the TE configuration with a period (L) of $2.4 \mu\text{m}$, duty cycle (F) of 0.7 , and thickness of gold (H_m) of 200 nm , in the domain of the wavelength (λ) and the height of the semiconductor stripes (H) for TE polarization (Fig. 2a), TM polarization (Fig. 2b), and unpolarized light (Fig. 2c). High transmittance exists in the range $\lambda > Ln_s$. Its short wavelength border is indicated by the white dashed line in Fig. 2a. In this region, called the deep-subwavelength region, only the zeroth diffraction order can be transmitted towards the air and substrate. Regions of high TE polarization transmittance (Fig. 2a) repeat as H increases [39], although this is not shown in the figure. We focus on the region with the smallest H enabling high transmittance, due to the simplicity of implementation of low H gratings. The region of transmittance of TE polarized light higher than 90% ranges above $5 \mu\text{m}$ with respect to wavelength and above $0.5 \mu\text{m}$ with respect to H . The transmittance of orthogonal TM polarization of light through the same grating is also substantial, and reaches above 60% in local maxima. Transmittance of the same polarization above 50% is present in a broad range of λ and H (see Fig. 2b). The transmittance of unpolarized light (Fig. 2c) follows the pattern of transmittance in the TE polarization map (Fig. 2a), indicating very high transmittance above 70% in a large area in the (λ, H) domain. It is noteworthy that although the configuration is not specifically optimized for maximal transmittance of unpolarized light, it still exhibits a remarkable level of unpolarized light transmittance that cannot be

achieved by the metalMHCG in the TM configuration analyzed in [43].

The electrical properties of the metalMHCG can be characterised by sheet resistance, estimated using the formula:

$$R_s = \frac{\rho L}{H_m a_m} = \frac{\rho}{H_m(1-F)} \quad (2)$$

where ρ is the electrical resistivity of the gold stripes. The second formula is valid in the case of rectangular cross-section of the semiconductor stripes. To accurately model the resistivity of gold stripes with nanoscale cross-sectional dimensions, it is necessary to consider the resistivity-size effect, which increases the electrical resistivity of the metalMHCG stripes above the level of the resistivity of bulk gold ($2.4 \cdot 10^{-8} \Omega \text{ m}$) [44]. In numerical calculations, we assume the resistivity of the golden stripes of the metalMHCG to be equal to the resistivity of bulk gold. Doing so, we determine the possible bottom limit of the metalMHCG sheet resistivity. It is important to note that in a realistic case metal stripes are expected to have lower conductivity compared to their bulk counterpart, due to possible impurities incorporated during fabrication, reduced crystal quality, contaminants or surfactants on the surface, and electron scattering. Applying formula 2, the sheet resistance of the configuration analysed in Fig. 2 is around $0.4 \Omega \text{ Sq}^{-1}$.

We shall now describe the methodology employed to find the optimal structure. To achieve maximal transmittance of TE polarized light, meticulous integration of the metal stripes with a semiconductor grating is necessary. The metal stripes should possess sufficient thickness to induce a waveguide effect, enabling the effective funnelling of radiation through the semiconductor stripes [39, 40]. On the other hand, excessive thickness of the metal stripes reduces the transmittance, due to absorption. Considering the interplay of these opposing effects, a global maximum in the transmittance of TE-polarized light can be attained by adjusting the quantity of metal in the metalMHCG structure.

We employ the multidimensional Nelder-Mead simplex algorithm [45] to search for the maximal transmittance of TE polarized light for a given value of metalMHCG sheet resistance. The variables considered in the optimization process are L, F, H, H_m . However, L, F, H_m are interrelated through Formula 2. In Fig. 3a, each point on the black curve represents a different configuration of the metalMHCG, obtained by maximizing the transmittance of TE polarized light. The TM polarized and unpolarized light transmittances corresponding to the metalMHCG configurations

are indicated by blue and green curves in the same figure. The black curve indicates that the global maximum of TE polarized light transmittance reaches 94.3%, which corresponds to sheet resistance of $0.58 \Omega \text{ Sq}^{-1}$. The transmittance of unpolarized light reaches a maximum value of approximately 74.2% for R_s of $2 \Omega \text{ Sq}^{-1}$. As the value of R_s decreases, the transmittance of unpolarized light gradually decreases, reaching 70% for $R_s = 0.28 \Omega \text{ Sq}^{-1}$. In the experimental analysis, our goal is to achieve the lowest possible sheet resistance while maintaining transmittance values close to the maximum. Therefore, we choose as the geometrical parameters of our target metalMHCG configuration $L = 2.394 \mu\text{m}$, $F = 0.71$, $H = 0.655 \mu\text{m}$, and $H_m = 0.2 \mu\text{m}$, which theoretically allow TE transmittance of 94.1%, unpolarised light transmittance of 71.1% and $R_s = 0.42 \Omega \text{ Sq}^{-1}$. Although this configuration exhibits a sheet resistance that is 40% lower than the configuration providing maximum TE transmittance, the transmittance is only 0.2% lower in comparison to the configuration with maximum TE transmittance.

Figure 3b maps the TE transmittance in the λ and H_m domain for the target configuration. Increasing the thickness of the gold stripes while keeping L , F , and H constant results in a narrowing of the high transmittance spectrum width and a shifting of the spectrum maximum towards shorter wavelengths with global maximum for $H_m = 0.2 \mu\text{m}$. The unpolarized transmittance shown in Fig. 3c follows a similar pattern to the TE transmittance map however maximal unpolarized transmittance reduces slowly with the increase in H_m . These trends will be observed in the forthcoming section on experimental implementation.

Experimental demonstration. Five configurations of the metalMHCG were fabricated by a combination of plasma enhanced chemical vapour deposition (PECVD), electron beam lithography (EBL), plasma etching by inductively coupled plasma-reactive ion etching (ICP-RIE), and e-beam physical vapour deposition (EBPVD). The configurations possess the same nominal grating parameters of $L = 2.40 \mu\text{m}$, $F = 0.71$, $H = 0.65 \mu\text{m}$ and five different thickness of the gold stripes ranging from 0.05 to 0.25 μm , with increments of 0.05 μm . The process of metalMHCG fabrication is described in Supplementary material, Section S1.

To prevent gold deposition on the semiconductor side walls, which could potentially reduce transmittance, the parameters of the ICP-RIE etching process were optimized to achieve a con-

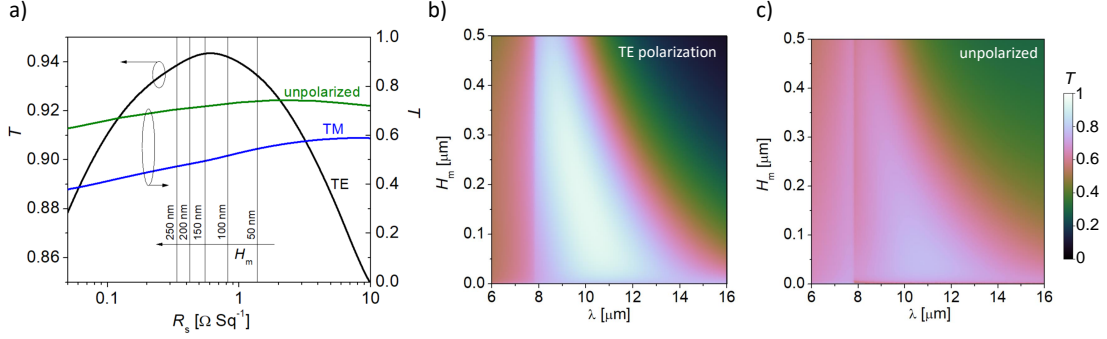


Figure 3: a) MetalMHCG maximal transmittance for TE polarization (black curve, left vertical axis) and corresponding transmittance of TM polarized (blue curve, right vertical axis) and unpolarized light (green curve, right vertical axis) as a function of the sheet resistance (R_s) of golden stripes. The black vertical lines indicate the thicknesses of the gold layers in the metalMHCG realised in the experimental part of this work. Maps of TE polarized b) and unpolarized light c) transmittance in the domain of the wavelength (λ) and thickness of the gold stripes (H_m) for metalMHCG with parameters $L = 2.394 \mu\text{m}$, $F = 0.71$, $H = 0.655 \mu\text{m}$.

cave side wall profile, as illustrated in Fig. 4a. Such a cross-section of the semiconductor stripes requires new optimal grating parameters that are different from the parameters of a rectangular cross section. Based on scanned SEM images, the metalMHCG cross-section was incorporated into a numerical optimisation algorithm (Fig. 4b) providing new dimensional parameters ($L = 2.51 \mu\text{m}$, $F = 0.68$, $H = 0.71 \mu\text{m}$). Figures 4a and 4b illustrate the graphical definition of F for the concave cross-section of the grating stripes. The TE and unpolarized transmittances for new grating parameters are nearly indistinguishable from the transmittance of metalMHCG with rectangular cross-sections for the same L , F , H and H_m .

The actual cross-section shape and dimensions of the processed metalMHCG were determined based on SEM images. All five samples with nominally different metal stripe thickness had the same geometrical parameters of the semiconductor grating: $L = 2.53 \mu\text{m}$, $F = 0.67$, and $H = 0.62 \mu\text{m}$, determined with a precision of 10 nm (comparison of calculated transmittance spectra of optimal configuration and realised are depicted in Supplementary material Fig. S4). The calculated spectra of TE transmittance (see Fig. 5a) exhibit maxima above 90% for the parameters and cross section of the processed metalMHCG. When the thickness of the gold stripes is increased from 50 nm to 250 nm, the wavelength of the calculated TE transmittance maxima shifts towards shorter wavelengths by $1.34 \mu\text{m}$. The metalMHCG with 200 nm thick gold stripes has a maximal calculated

TE transmittance of 95.6% at a wavelength of $8.6 \mu\text{m}$. The calculated unpolarized transmittance (Fig. 5b) follows the behaviour of TE transmittance, as the spectrum of TM transmittance is a slowly varying function of wavelength in the spectral range under consideration, as seen in the inset of Fig. 5b. The maximum of calculated unpolarized transmittance is achieved for metalMHCG with $H_m = 50 \text{ nm}$ and reaches above 70% at a wavelength of $10 \mu\text{m}$. As the thickness of the metal increases, the transmittance of unpolarized light decreases, mainly due to the decrease in TM transmittance (see inset in Fig. 5b).

Figure 5c presents the measured TE transmittance spectra for the five metalMHCG samples. The description of the experimental setup for transmittance measurements and the experimental method are detailed in Supplementary material, Section S2. The spectra show a maximum that shifts towards shorter wavelengths by $1.21 \mu\text{m}$ as the gold stripe thickness increases from 50 nm to 250 nm. The maximal TE transmittance is achieved for a metalMHCG with 200 nm thick gold stripes, reaching 92% at a wavelength of $9.08 \mu\text{m}$ which corresponds to relative TE transmittance of 133%. The bandwidth of relative transmittance exceeding 100% is $3.03 \mu\text{m}$. In the deep-subwavelength regime corresponding to wavelengths longer than $8 \mu\text{m}$, the TM transmittance is from 50% to slightly above 60% and varies slightly (see the inset in Fig. 5d). Figure 5d shows the unpolarized transmittance spectra for the five considered samples. The configuration

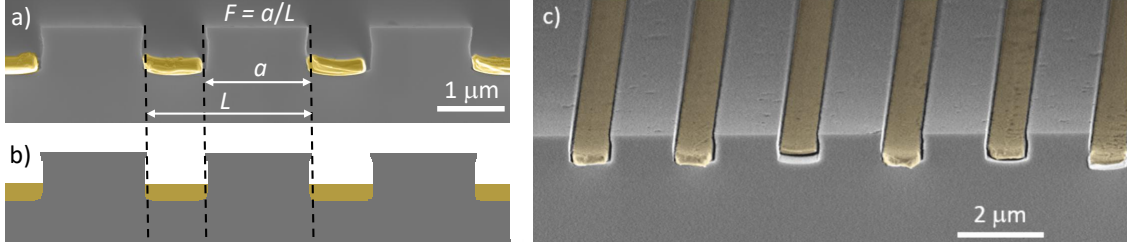


Figure 4: a) Cross-section scanning electron microscope (SEM) image of metalMHCg; b) image of the metalMHCg implemented in the numerical algorithm; c) tilted SEM image of cleaved edge of metalMHCg. The thickness of the gold stripes is 200 nm in all images.

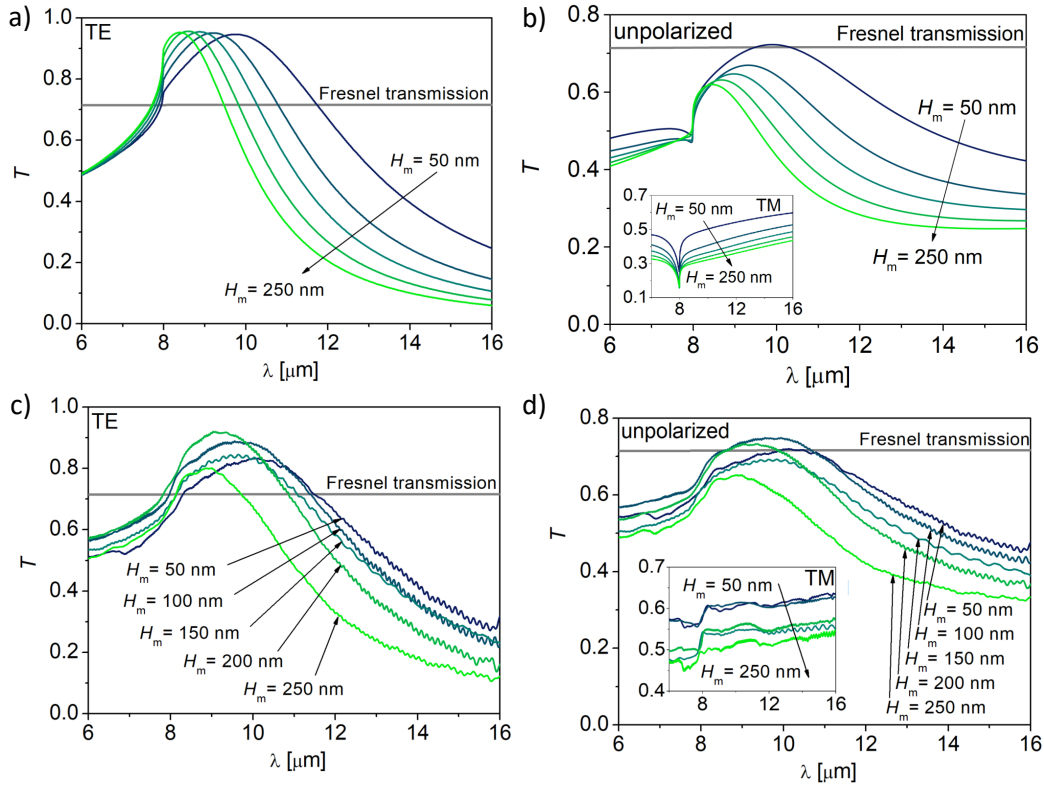


Figure 5: Calculated a, b) and measured c, d) transmittance spectra of metalMHCg in the case of TE-polarized a, c) and unpolarized b, d) light incidence. The spectra are calculated for real-world cross-sections of semiconductor and metal stripes with the geometrical parameters of the metalMHCg determined by SEM images ($L = 2.53 \mu\text{m}$, $F = 0.67$, and $H = 0.62 \mu\text{m}$) and H_m from 50 nm to 250 nm indicated by different colours. The same colours correspond to measured spectra of samples with the same thickness of gold stripes. The grey line represents Fresnel transmittance through the planar interface between the GaAs and air, based on GaAs refractive index dispersion [41]. The insets in b) and d) illustrate TM transmittance of the metalMHCg.

with a gold stripe thickness of 100 nm shows a maximum level of 75%, which corresponds to relative transmittance of 108% with an above 100% relative transmittance bandwidth of $2.03 \mu\text{m}$. The discussed properties of the metalMHCg experimental spectra are in good agreement with the

simulations. The inconsistencies, mainly concerning the level of transmittance, are typically related to the fabrication precision influencing grating stripes roughness. Therefore, the experimental transmittance can be enhanced by improving the process of metalMHCg fabrication. The ex-

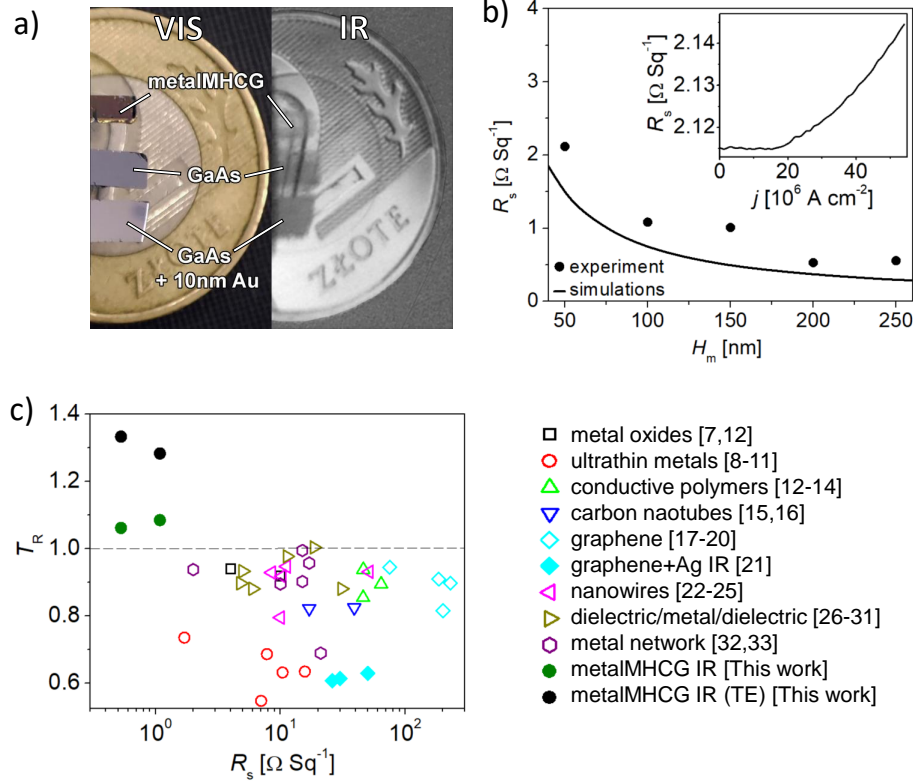


Figure 6: a) Pictures of three samples from the same GaAs wafer: metalMHCG on the GaAs substrate (metalMHCG), bare GaAs substrate (GaAs), and GaAs substrate with a 10-nm thick gold layer on the surface (GaAs + 10 nm Au). The pictures are shown in visible light (VIS) and in long-wavelength infrared (IR), with a coin in the background heated to 48°C, corresponding to the spectral maximum of black body radiation at a wavelength of 9 μm ; b) measured sheet resistance of the metalMHCG (indicated by dots) with varying thicknesses of gold stripes from 50 nm to 200 nm with 50 nm steps. The simulated sheet resistance for a corresponding range of gold stripe thicknesses is represented by the black line. Inset illustrates measured dependence of sheet resistance versus current density; c) TE polarized (black dots) and unpolarized (green dots) optical relative transmittance (T_R) versus sheet resistance for the metalMHCG with the best performance (from this work). The performances of TCEs based on other approaches are indicated by all other symbols and colors. References to works describing TCEs and their characteristics are indicated in the legend. The full symbols represent relative transmittance at a wavelength of $\sim 9 \mu\text{m}$, the open symbols represent maximal relative transmittance in the visible range.

perimental unpolarized transmittance is slightly larger than the theoretical one. We hypothesise that this may be caused by the nonperfect flatness of the gold stripes walls reducing possible plasmonic effects and hence reducing absorption of TM polarization and contributing to higher transmittance. Overall, our experimental results show very good agreement with the calculations and confirm the feasibility of high-power transmittance using a metalMHCG. Photographs of the fabricated metalMHCG on GaAs substrate, along with plain GaAs substrate and a 10-nm thick gold layer on GaAs substrate, are presented in Fig. 6a. The

high transparency of the metalMHCG is evident in infrared light (IR), surpassing the transmission through the plain GaAs substrate. On the other hand, the 10-nm thick gold layer on the GaAs substrate enables only 2% transmittance, which is nontransparent to infrared light—as is clearly evident in the photography.

Determination of metalMHCG sheet resistance (R_s) required the fabrication of separate samples. The electrical resistance of the metalMHCG samples used for optical characterisation was significantly below the error of the measurement setup. To minimize the characterisation error, we de-

signed the resistance of the metalMHCs to be $\sim 100 \Omega$. The resistances of the samples were at least three orders of magnitude higher than the measurement error. The samples made for electrical characterisation consisted of 12, 6, 4, 4, and 2 stripes with different gold thicknesses from 50 nm to 250 nm with a 50 nm step and the stripes were 2 mm in length. An example configuration is presented in Supplementary material, Fig. S3. The gold stripes were placed on an undoped GaAs substrate. The electrical connection was facilitated by electrical pads, positioned at both ends of the stripes. Based on the current-voltage characteristics and geometric dimensions of the gold stripes, the sheet resistance was determined for all samples. The sheet resistance is shown in Fig. 6b, along with the theoretical values calculated assuming the bulk gold resistance. The sheet resistances of the metalMHCs that exhibited the maximal unpolarized and TE transmittances, with 100 nm and 200 nm gold stripe thicknesses, were $1 \Omega \text{Sq}^{-1}$ and $0.5 \Omega \text{Sq}^{-1}$ respectively. The measured resistance of the gold stripes was approximately $3.5 \cdot 10^{-8} \Omega \text{m}$, which is 45% larger than the bulk gold conductivity. The dependence of sheet resistance on the current flowing through metalMHCG was also determined. The generated Joule heat increases the temperature of the stripes, which increases the sheet resistance. The dependence of sheet resistance on current density for the metalMHCG with 50-nm thick gold stripes is shown in the inset of Fig. 6b. A noticeable increase in sheet resistance occurs at current densities above $2 \cdot 10^7 \text{ A cm}^{-2}$. An increase in sheet resistance can be expected at higher current densities for samples with thicker gold stripes.

A more general comparison of the optical and electrical performance of the metalMHCG and numerous configurations of TCEs reported so far is presented in Fig. 6c. If the relative transmittance of TCEs from other studies were not directly indicated, they were derived by taking into account their experimentally measured absolute transmittance and the refractive index of the substrates. Among the various TCEs, $\text{Al}_2\text{O}_3\text{-Cu:Ag-ZnO}$ [31] and Cu nanotrrough networks [33] have exhibited the largest transmittivity to date, with their relative transmittance either slightly surpassing or approaching 100%. In terms of electrical properties, the lowest sheet resistance has been achieved by a Cu nanotrrough network [33], FTO [12], dielectric-metal-dielectric electrodes composed of AZO-Ag-AZO [27], and $\text{MoO}_3\text{-Ag-MoO}_3$ [28]. These TCEs exhibit sheet resistances ranging from $2 \Omega \text{Sq}^{-1}$ to $6 \Omega \text{Sq}^{-1}$. Conductive composite films based on silver nanowires and graphene measured in in-

frared range demonstrate relative transmittance over 60% (absolute transmittance of 70%) and sheet resistance of $28 \Omega \text{Sq}^{-1}$ [21]. The numerically calculated infrared transmittivities of TCEs implemented on high refractive index substrate are presented in Supplementary material, Fig. S5. The calculations reveal that TCEs based on ITO, AZO, FTO, metal plates, and grids reach the level of Fresnel transmittance when their sheet resistance exceeds $100 \Omega \text{Sq}^{-1}$. Notably, graphene layers demonstrate exceptional performance in this context, reaching Fresnel transmittance for sheet resistance significantly below $100 \Omega \text{Sq}^{-1}$.

In this context, metalMHCs exhibit substantial superiority over other TCEs in terms of both optical transmittance and electrical properties, as supported by theoretical and empirical evidence. The sheet resistance of the metalMHCs is 4 times smaller compared to the best performing TCEs. Additionally, their polarized and unpolarized transmittances surpass the threshold of Fresnel transmittance, a feat that is difficult to achieve for other TCEs.

3 Discussion

In this research, we performed an experimental demonstration of a monolithic high contrast grating integrated with metal stripes (metalMHCG). The high transmittance of transverse electric (TE) polarization through the metalMHCG was enabled by the funnelling the light through semiconductor stripes that reduced reflection and absorption of the light by the metal stripes. This mechanism enabled transmittance of 92% in our experiment, which corresponds to 130% of relative transmittance. To our best knowledge, this is the record for transmittance demonstrated through a transparent conductive electrode (TCE). The structure shows $3 \mu\text{m}$ bandwidth above 100% relative transmittance for polarized light. The metalMHCG in the TE configuration that was considered in this work reveals weak polarization selectivity and enables significant transmittance of transverse magnetic (TM) polarization, which is enabled by the low-quality factor resonance located in the air slits between the semiconductor stripes. Transmittance of TM polarization is 50–60% in a wide spectral range around maximal TE transmittance, leading to 75% transmittance of unpolarized light corresponding to 108% of relative transmittance. This is also the record value ever reported. The corresponding sheet resistance of the metalMHCG is $1 \Omega \text{Sq}^{-1}$. Another configuration achieved absolute and relative transmittances of 73% and 106%, respectively, and a record low sheet re-

sistance of $0.5 \Omega \text{Sq}^{-1}$, surpassing the best experimental results and theoretical predictions for other TCEs over fourfold. All experimental results presented in this paper exhibit excellent agreement with theory, which predicted only a slightly different transmittance and 30% – 40% lower sheet resistance compared to our experimental results. Nevertheless, it exhibits a remarkably low sheet resistivity, attributed to the unique capacity of the metalMHCG to accommodate a significantly larger volume of metal compared to any other TCE. The increased metal content does not compromise the light transmittance through the metalMHCG, due to the light funnelling mechanism which minimizes the interaction of the electromagnetic field with the metal and eliminates Fresnel reflection.

The underlying motivation for this research arose from the need for efficient methods for the development of transparent electrodes with the capability to inject high-density current into semiconductors across large electrode areas. This study presents a novel approach towards the realization of optically transparent and highly electrically conductive structures, which can be seamlessly integrated monolithically with various materials employed in optoelectronics, particularly those composed of high refractive index semiconductors. The metalMHCG configuration exhibits the ability to facilitate light transmittance spanning a broad spectral range, from ultraviolet to infrared [39]. Achieving high transmittance of infrared light is particularly challenging due to much higher free carrier absorption in comparison to the visible range. The exceptional properties of the metalMHCG, coupled with the promise of high-density current injection into semiconductors pave the way for significant advancements in the efficiency of electroluminescent diodes, photodiodes, and semiconductor lasers. These properties also open new possibilities for innovative applications beyond the traditional uses of these devices.

Acknowledgments

MM acknowledges the support from the Polish National Science Center, grant OPUS 2019/33/B/ST7/02591. AS and ME acknowledge the support by the statutory funds of the Łukasiewicz Research Network – Institute of Microelectronics and Photonics. This work has been completed while WG and KB were the Doctoral Candidate in the Interdisciplinary Doctoral School at the Lodz University of Technology, Poland.

References

- [1] Jan P.F. Lagerwall and Giusy Scalia. A new era for liquid crystal research: Applications of liquid crystals in soft matter nano-, bio- and microtechnology. *Current Applied Physics*, 12(6):1387–1412, 2012.
- [2] Malte C. Gather, Anne Köhnen, and Klaus Meerholz. White organic light-emitting diodes. *Advanced Materials*, 23(2):233–248, 2010.
- [3] Xi Yang, Wenqing Liu, Min Xiong, Yingying Zhang, Tao Liang, Jingting Yang, Mingsheng Xu, Jian Ye, and Hongzheng Chen. Au nanoparticles on ultrathin mos2sheets for plasmonic organic solar cells. *J. Mater. Chem. A*, 2(36):14798–14806, 2014.
- [4] David A Rider, Ryan T Tucker, Brian J Worfolk, Kathleen M Krause, Abeed Lalany, Michael J Brett, Jillian M Buriak, and Kenneth D Harris. Indium tin oxide nanopillar electrodes in polymer/fullerene solar cells. *Nanotechnology*, 22(8):085706, 2011.
- [5] Akshay Kumar and Chongwu Zhou. The race to replace tin-doped indium oxide: Which material will win? *ACS Nano*, 4(1):11–14, 2010.
- [6] Radhouane Bel Hadj Tahar, Takayuki Ban, Yutaka Ohya, and Yasutaka Takahashi. Tin doped indium oxide thin films: Electrical properties. *Journal of Applied Physics*, 83(5):2631–2645, 1998.
- [7] Bon-Ryul Koo, Dong-Hyeun Oh, Doh-Hyung Riu, and Hyo-Jin Ahn. Improvement of transparent conducting performance on oxygen-activated fluorine-doped tin oxide electrodes formed by horizontal ultrasonic spray pyrolysis deposition. *ACS Applied Materials & Interfaces*, 9(51):44584–44592, 2017.
- [8] Guiying Xu, Liang Shen, Chaohua Cui, Shanpeng Wen, Rongming Xue, Weijie Chen, Haiyang Chen, Jingwen Zhang, Hongkun Li, Yaowen Li, and et al. High-performance colorful semitransparent polymer solar cells with ultrathin hybrid-metal electrodes and fine-tuned dielectric mirrors. *Advanced Functional Materials*, 27(15):1605908, 2017.
- [9] Yan-Gang Bi, Yue-Feng Liu, Xu-Lin Zhang, Da Yin, Wen-Quan Wang, Jing Feng, and Hong-Bo Sun. Ultrathin metal films as the transparent electrode in ito-free organic optoelectronic devices. *Advanced Optical Materials*, 7(6):1800778, 2019.

- [10] Ch Surya Prakasarao, Pratim Hazarika, Slavia Deeksha DSouza, Jean Maria Fernandes, M. Kovendhan, R. Arockia Kumar, and D. Paul Joseph. Investigation of ultrathin and flexible au–ag–au transparent conducting electrode. *Current Applied Physics*, 20(10):1118–1124, 2020.
- [11] Chu-Chen Chueh, Shang-Chieh Chien, Hin-Lap Yip, José Francisco Salinas, Chang-Zhi Li, Kung-Shih Chen, Fang-Chung Chen, Wen-Chang Chen, and Alex K.-Y. Jen. Toward high-performance semi-transparent polymer solar cells: Optimization of ultra-thin light absorbing layer and transparent cathode architecture. *Advanced Energy Materials*, 3(4):417–423, 2012.
- [12] Aman Anand, Md Moidul Islam, Rico Meitzner, Ulrich S. Schubert, and Harald Hoppe. Introduction of a novel figure of merit for the assessment of transparent conductive electrodes in photovoltaics: Exact and approximate form. *Advanced Energy Materials*, 11(26):2100875, 2021.
- [13] Nara Kim, Seyoung Kee, Seoung Ho Lee, Byoung Hoon Lee, Yung Ho Kahng, Yong-Ryun Jo, Bong-Joong Kim, and Kwanghee Lee. Highly conductive pedot:pss nanofibrils induced by solution-processed crystallization. *Advanced Materials*, 26(14):2268–2272, 2013.
- [14] Michael Vosgueritchian, Darren J. Lipomi, and Zhenan Bao. Highly conductive and transparent pedot:pss films with a fluorosurfactant for stretchable and flexible transparent electrodes. *Advanced Functional Materials*, 22(2):421–428, 2011.
- [15] Il Jeon, Clement Delacou, Hiroshi Okada, Graham E. Morse, Tae-Hee Han, Yuta Sato, Anton Anisimov, Kazu Suenaga, Esko I. Kaupinen, Shigeo Maruyama, and et al. Polymeric acid-doped transparent carbon nanotube electrodes for organic solar cells with the longest doping durability. *Journal of Materials Chemistry A*, 6(30):14553–14559, 2018.
- [16] Farhad Daneshvar, Stefano Tagliaferri, Hengxi Chen, Tan Zhang, Cong Liu, and Hung-Jue Sue. Ultralong electrospun copper–carbon nanotube composite fibers for transparent conductive electrodes with high operational stability. *ACS Applied Electronic Materials*, 2(9):2692–2698, 2020.
- [17] Zhike Liu, Peng You, Shenghua Liu, and Feng Yan. Neutral-color semitransparent organic solar cells with all-graphene electrodes. *ACS Nano*, 9(12):12026–12034, 2015.
- [18] Dong Hee Shin, Chan Wook Jang, Ha Seung Lee, Sang Woo Seo, and Suk-Ho Choi. Semi-transparent flexible organic solar cells employing doped-graphene layers as anode and cathode electrodes. *ACS Applied Materials & Interfaces*, 10(4):3596–3601, 2018.
- [19] Ju Hwan Kang, Sukyung Choi, Yu Jung Park, Jin Sung Park, Nam Sung Cho, Shinuk Cho, Bright Walker, Dong Soo Choi, Jin-Wook Shin, and Jung Hwa Seo. Cu/graphene hybrid transparent conducting electrodes for organic photovoltaic devices. *Carbon*, 171:341–349, 2021.
- [20] Xing Huang, Peng Sheng, Zeyi Tu, Fengjiao Zhang, Junhua Wang, Hua Geng, Ye Zou, Chong-an Di, Yuanping Yi, Yimeng Sun, and et al. A two-dimensional π -d conjugated coordination polymer with extremely high electrical conductivity and ambipolar transport behaviour. *Nature Communications*, 6(1), 2015.
- [21] Shengyong Wang, Huan Liu, Yongqiang Pan, Minyu Bai, Fei Xie, Jijie Zhao, Kaihao Xue, Shuai Wen, and Peng Chen. Demonstration of wide spectrum transparent conductive composite films based on silver nanowires and graphene. *Infrared Physics & Technology*, 124:104172, 2022.
- [22] Jung-Yong Lee, Stephen T. Connor, Yi Cui, and Peter Peumans. Solution-processed metal nanowire mesh transparent electrodes. *Nano Letters*, 8(2):689–692, 2008.
- [23] Huizhang Guo, Na Lin, Yuanzhi Chen, Zhenwei Wang, Qingshui Xie, Tongchang Zheng, Na Gao, Shuping Li, Junyong Kang, Duanjun Cai, and et al. Copper nanowires as fully transparent conductive electrodes. *Scientific Reports*, 3(1), 2013.
- [24] Po-Chun Hsu, Desheng Kong, Shuang Wang, Haotian Wang, Alex J. Welch, Hui Wu, and Yi Cui. Electrolessly deposited electrospun metal nanowire transparent electrodes. *Journal of the American Chemical Society*, 136(30):10593–10596, 2014.
- [25] Fei Guo, Ning Li, Vuk V. Radmilović, Velimir R. Radmilović, Mathieu Turbiez, Erdmann Spiecker, Karen Forberich, and Christoph J. Brabec. Fully printed organic

- tandem solar cells using solution-processed silver nanowires and opaque silver as charge collecting electrodes. *Energy & Environmental Science*, 8(6):1690–1697, Mar 2015.
- [26] L. Cattin, A. El Mahlali, M.A. Cherif, S. Touihri, Z. El Jouad, Y. Mouchaal, P. Blanchard, G. Louarn, H. Essaidi, M. Addou, and et al. New dielectric/metal/dielectric electrode for organic photovoltaic cells using cu:al alloy as metal. *Journal of Alloys and Compounds*, 819:152974, 2020.
- [27] M. Acosta, J. Mendez-Gamboa, I. Riech, C. Acosta, and M. Zambrano. Azo/ag/azo multilayers electrodes evaluated using a photonic flux density figure of merit for solar cells applications. *Superlattices and Microstructures*, 127:49–53, 2019.
- [28] Linda Cattin, Guy Louarn, Mustapha Morsli, and Jean Christian Bernède. Semi-transparent organic photovoltaic cells with dielectric/metal/dielectric top electrode: Influence of the metal on their performances. *Nanomaterials*, 11(2):393, 2021.
- [29] Y. Mouchaal, G. Louarn, A. Khelil, M. Morsli, N. Stephant, A. Bou, T. Abachi, L. Cattin, M. Makha, P. Torchio, and et al. Broadening of the transmission range of dielectric/metal multilayer structures by using different metals. *Vacuum*, 111:32–41, 2015.
- [30] Areum Kim, Yulim Won, Kyoohye Woo, Sunho Jeong, and Jooho Moon. All-solution-processed indium-free transparent composite electrodes based on ag nanowire and metal oxide for thin-film solar cells. *Advanced Functional Materials*, 24(17):2462–2471, 2014.
- [31] Chengang Ji, Dong Liu, Cheng Zhang, and L. Jay Guo. Ultrathin-metal-film-based transparent electrodes with relative transmittance surpassing 100 *Nature Communications*, 11(1), 2020.
- [32] K. D. Rao, Christoph Hunger, Ritu Gupta, Giridhar U. Kulkarni, and Mukundan Thelakkat. A cracked polymer templated metal network as a transparent conducting electrode for ito-free organic solar cells. *Physical Chemistry Chemical Physics*, 16(29):15107–15110, Jun 2014.
- [33] Hui Wu, Desheng Kong, Zhichao Ruan, Po-Chun Hsu, Shuang Wang, Zongfu Yu, Thomas J. Carney, Liangbing Hu, Shanhui Fan, and Yi Cui. A transparent electrode based on a metal nanotrough network. *Nature Nanotechnology*, 8(6):421–425, 2013.
- [34] Tian Fang, Aniruddha Konar, Huili Xing, and Debdeep Jena. Carrier statistics and quantum capacitance of graphene sheets and ribbons. *Applied Physics Letters*, 91(9), 2007.
- [35] Neng Ye, Jieli Yan, Shuang Xie, Yuhan Kong, Tao Liang, Hongzheng Chen, and Mingsheng Xu. Silver nanowire–graphene hybrid transparent conductive electrodes for highly efficient inverted organic solar cells. *Nanotechnology*, 28(30):305402, 2017.
- [36] S. Krause, P.-T. Miclea, F. Steudel, S. Schweizer, and G. Seifert. Few micrometers wide, perfectly isolating scribes in transparent conductive oxide layers prepared by femtosecond laser processing. *Journal of Renewable and Sustainable Energy*, 6(1), 2014.
- [37] Kristupas Kazimieras Tikuišis, Adam Dubroka, Klára Uhlířová, Florian Speck, Thomas Seyller, Maria Losurdo, Milan Orlita, and Martin Veis. Dielectric function of epitaxial quasi-freestanding monolayer graphene on si-face 6h-sic in a broad spectral range. *Physical Review Materials*, 7(4), 2023.
- [38] Nicolas Massonnet, Alexandre Carella, Olivier Jaudouin, Patrice Rannou, Gautier Laval, Caroline Celle, and Jean-Pierre Simonato. Improvement of the seebeck coefficient of p-dot:pss by chemical reduction combined with a novel method for its transfer using free-standing thin films. *Journal of Materials Chemistry C*, 2(7):1278–1283, Oct 2014.
- [39] Tomasz Czyszanowski, Adam K. Sokół, Maciej Dems, and Michał Wasiak. Transparent electrode employing deep-subwavelength monolithic high-contrast grating integrated with metal. *Optics Express*, 28(19):28383, 2020.
- [40] Adam K. Sokół and Tomasz Czyszanowski. Nearly perfect transmission of unpolarized infrared radiation through a one-dimensional metal grating embedded in a monolithic high-contrast grating. *Optics Express*, 28(26):38857, 2020.
- [41] T. Skauli, P. S. Kuo, K. L. Vodopyanov, T. J. Pinguet, O. Levi, L. A. Eyres, J. S. Harris, M. M. Fejer, B. Gerard, L. Becouarn, and et al. Improved dispersion relations for gaas and applications to nonlinear optics. *Journal of Applied Physics*, 94(10):6447–6455, 2003.

- [42] Mark A. Ordal, Robert J. Bell, Ralph W. Alexander, Larry L. Long, and Marvin R. Querry. Optical properties of au, ni, and pb at submillimeter wavelengths. *Applied Optics*, 26(4):744, 1987.
- [43] Landobasa Y. Tobing, Michał Wasiak, Dao Hua Zhang, Weijun Fan, and Tomasz Czyszanowski. Nearly total optical transmission of linearly polarized light through transparent electrode composed of gasb monolithic high-contrast grating integrated with gold. *Nanophotonics*, 10(15):3823–3830, 2021.
- [44] T.H. Gilani and Dian Rabchuk. Electrical resistivity of gold thin film as a function of film thickness. *Canadian Journal of Physics*, 96(3):272–274, 2018.
- [45] Margaret Wright. *Direct search methods: Once scorned, now respectable*, pages 191–208. Addison-Wesley, 1996.

Supplementary materials

Monolithic High Contrast Grating Integrated with Metal: A Transparent Conductive Electrode for Infrared Optoelectronics with Exceptionally High Conductivity and Transmittivity

Marek Ekielski¹, Weronika Głowadzka², Karolina Bogdanowicz^{1,2}, Michał Rygała³, Monika Mikulicz³, Patrycja Śpiewak², Marcin Kowalski⁴, Marcin Gębski², Marcin Motyka³, Anna Szerling¹, and Tomasz Czyszanowski^{2,*}

¹*Lukasiewicz Research Network - Institute of Microelectronics and Photonics, al. Lotników 32/46, 02-668 Warsaw, Poland*

²*Photonics Group, Institute of Physics, Lodz University of Technology, ul. Wolczanska 219, 90-924 Łódź, Poland*

³*Laboratory for Optical Spectroscopy of Nanostructures, Department of Experimental Physics, Faculty of Fundamental Problems of Technology, Wrocław University of Science and Technology, Wybrzeże Wyspiańskiego 27, 50-370 Wrocław, Poland*

⁴*Institute of Optoelectronics, Military University of Technology, Gen. S. Kaliskiego, 00-908 Warsaw, Poland*
**Corresponding author: tomasz.czyszanowski@p.lodz.pl*

August 8, 2023

This PDF file includes:

- Supporting figures [S1-S5](#)
- Supporting information [S1](#), [S2](#)

S1 Fabrication of metalMHCG

The metalMHCG structure was fabricated using a combination of plasma enhanced chemical vapour deposition (PECVD), electron beam lithography (EBL), inductively coupled plasma-reactive ion etching (ICP-RIE), and e-beam physical vapor deposition (EBPVD), following the technological steps illustrated in Fig. S1. First, the top of a double-sided polished GaAs substrate was covered with a triple layer consisting of SiO₂/Cr/SiO₂, to act as an etch mask. The thicknesses of the three layers of SiO₂/Cr/SiO₂ were 200 nm, 30 nm, and 20 nm, respectively (Fig. S1a). The prepared substrate was then spin-coated with a 200-nm thick layer of AR-P 6200.9 e-beam resist, followed by EBL patterning and development in AR 600-546 for 60 s at 22°C (Fig. S1b). The EBL-fabricated pattern, representing the desired MHCG design, was then transferred sequentially by plasma etching to a 20-nm thick SiO₂ layer (Fig. S1c), a 30-nm thick Cr layer (Fig. S1d), and finally to a 200-nm thick SiO₂ layer (Fig. S1e) that served as the main GaAs etch mask. The SiO₂ layers were etched using CHF₃/CF₄ chemistry at a temperature of 20°C, 100 W RF power, and a chamber pressure of mTorr 20 mTorr. The Cr layer was etched using Cl₂/O₂ chemistry at 20°C, with a PICP of 800 W, PRF of 50 W, and chamber pressure of 10 mTorr. The upper layer of SiO₂ (20 nm thick) and the layer of Cr were sacrificial layers that allowed the EBL-fabricated pattern to be transferred to the lower SiO₂ layer (200 nm thick) etch mask. The GaAs substrate was then plasma etched (Fig. S1f) using BCl₃/Ar chemistry at a temperature of 10°C, with a PICP of 180 W, PRF of 100 W, and a chamber pressure of 5 mTorr, resulting in slightly concave profiles of the etched side walls. The SiO₂ hard mask remaining unetched. The substrate was then diced into 5×5mm samples, and selected samples were e-beam evaporated with gold (Fig. S1g), with thicknesses ranging from 50 nm to 250 nm in 50 nm increments. The fabrication process was completed by removing the SiO₂ hard mask (Fig. S1h) and covering the metalMHCG structure with a layer of Au, deposited on top using buffered hydrofluoric acid (BOE) solution.

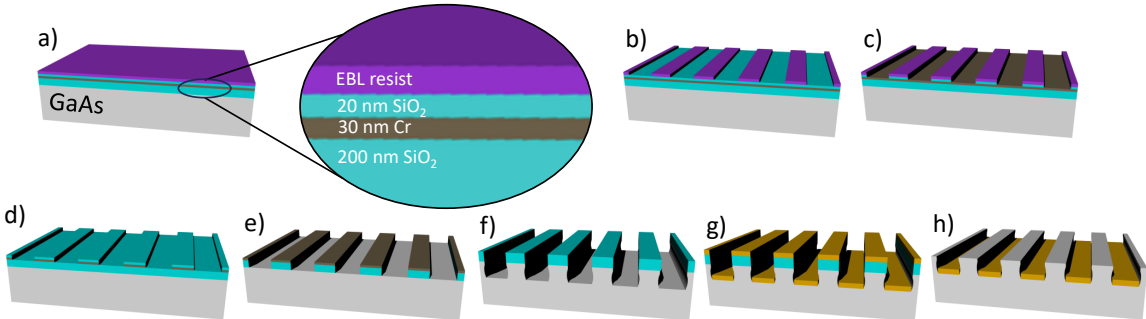


Figure S1: Flow chart of metalMHCG fabrication steps: a) double side polished GaAs wafer covered with set of mask layers and electron beam sensitive resist; b) EBL fabricated pattern; c) pattern transfer to upper SiO₂ layer; d) pattern transfer to Cr layer; e) pattern transfer to lower SiO₂ layer; f) pattern transfer to GaAs substrate; g) Au e-beam evaporation and SiO₂ mask lift-off; h) fabricated GaAs-Au metalMHCG structure.

The first generation of metalMHCGs had the expected concave cross-section of the side walls, similar to those presented in Fig. 4a, spatial parameters (L, F, H) close to the designed parameters. However, the non-rectangular cross-section of the semiconductor stripes resulted in a shift of the transmittance maximum relative to the expected wavelength, leading to a maximum transmittance of polarized light of only 80%. To optimize the transmittance through the metalMHCG, we used scanning electron microscopy (SEM) images to accurately capture the cross-section of the semiconductor and metal stripes.

S2 Transmittance measurements

Transmittance measurements were conducted using a Vertex 80v vacuum Fourier Transform Infrared spectrometer (FTIR) from Bruker. Due to the many limitations and difficulties of working in the mid-infrared spectral region, it was necessary to use a Fourier spectrometer instead of a simpler monochromator-based setup. The advantages of using the FTIR approach over the dispersive setup have been extensively studied and described [S1, S2]. Figure S2a shows the experimental setup for transmittance measurements. The sample light generated by a polychromatic source (either a halogen or a glow bar, depending on the spectral range) was guided by parabolic golden mirrors to the Michelson interferometer and then focused onto the sample at a normal incident angle, creating a roughly 1-mm diameter spot entirely contained within the 5×5 mm metalMCHG sample. The sample was placed on a mounting holder with a slit slightly larger than the diameter of the focused spot, which allowed light to transmit through the entire sample and exit from the etched grating. The transmitted light was then directed to a HgCdTe (MCT) liquid-nitrogen cooled detector and transferred as an electrical response into an analog-to-digital converter. The signal was later modified using a 3-Term Blackman-Harris apodization function or an adequate zero-filling factor and converted into a spectrum using Fast Fourier Transform. To perform polarization-resolved measurements, a KRS-5 wire-grid polarizer was inserted into the beam path before the light reached the sample, as shown in Fig. 1b. Using this experimental procedure, we were able to obtain spectra in the 1.3 - $16 \mu\text{m}$ spectral range with a 4 cm^{-1} resolution [S3, S4].

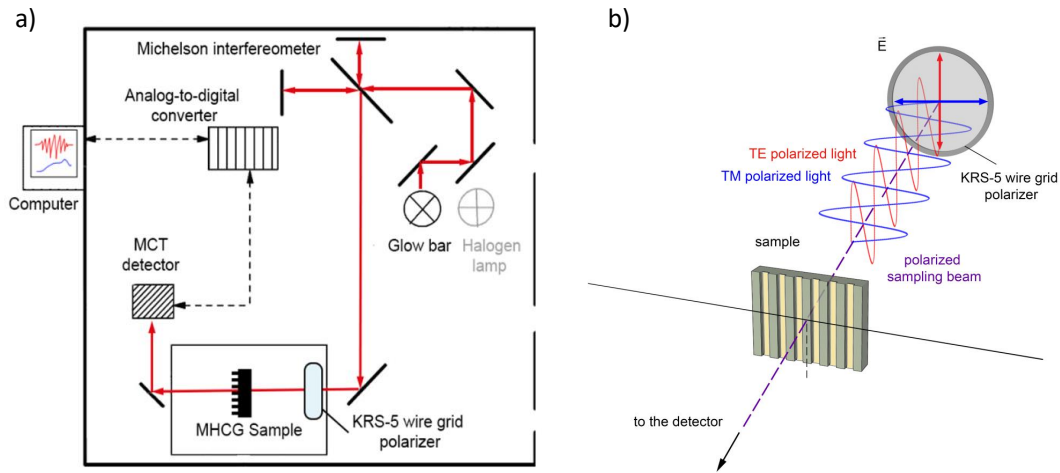


Figure S2: a) Schematic view of the beam path in a transmittance experiment with FTIR setup; b) close-up of polarizer mounting showing the direction of stripes in the sample.

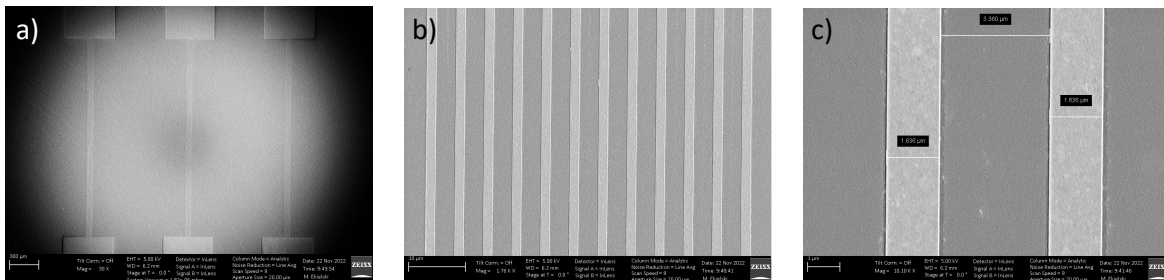


Figure S3: Top view scanning electron microscope (SEM) images at various degrees of magnification. Images show structures with 50-nm thick metal stripes prepared for electrical characterisation.

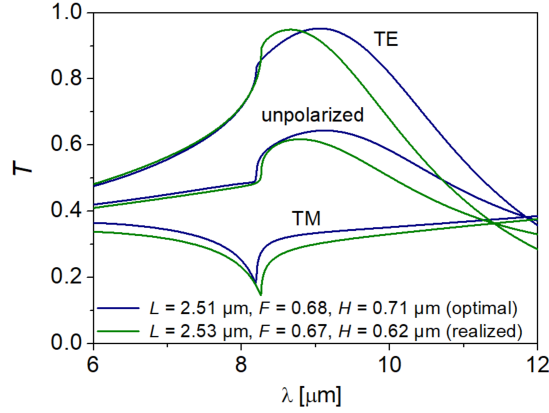


Figure S4: Calculated transmittance spectra of metalMHCg in the case of TE-polarized (TE), TM-polarized (TM) and unpolarized light incidence. The spectra are calculated for real-world cross-sections of semiconductor and metal stripes with the geometrical parameters indicated in the figure and $H_m = 200$ nm. Blue represents optimal configuration and green the configuration realised in the experiment.

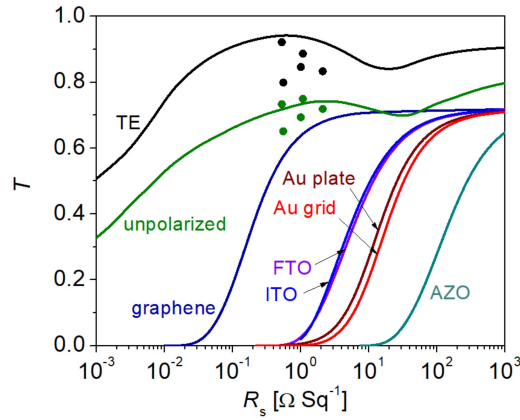


Figure S5: Measured absolute transmittance versus sheet resistance of metalMHCgs measured in this work for TE polarized (black dots) and unpolarized light (green dots). Black and green lines represent the calculated dependences of absolute transmittance for the GaAs-based metalMHCg versus sheet resistance for TE transmittance and unpolarized transmittance, respectively. Other lines represent calculated absolute transmittance for graphene, metal oxide, gold plate, and gold grids all deposited on GaAs wafer versus sheet resistance for their refractive indices corresponding to the infrared spectral range and lowest reported resistivities [S5–S12]

References

- [S1] Thermofisher.com. <https://assets.thermofisher.com/TFS-Assets/LSG/Application-Notes/TN50674-E-0215M-FT-IR-Advantages.pdf>. Accessed: 2023-07-21.
- [S2] Peter R. Griffiths and De Haseth James A. *Fourier transform infrared spectrometry*. Wiley, 2007.
- [S3] M Motyka, G Sęk, F Janiak, J Misiewicz, K Kłos, and J Piotrowski. Fourier-transformed photoreflectance and fast differential reflectance of hgcdte layers. the issues of spectral resolution and fabry-perot oscillations. *Measurement Science and Technology*, 22(12):125601, 2011.

- [S4] Marcin Motyka and Jan Misiewicz. Fast differential reflectance spectroscopy of semiconductor structures for infrared applications by using fourier transform spectrometer. *Applied Physics Express*, 3(11):112401, 2010.
- [S5] Yu Wang, Adam C. Overvig, Sajan Shrestha, Ran Zhang, Ren Wang, Nanfang Yu, and Luca Dal Negro. Tunability of indium tin oxide materials for mid-infrared plasmonics applications. *Optical Materials Express*, 7(8):2727, 2017.
- [S6] Mansour S. Farhan, Erfan Zalnezhad, Abdul Razak Bushroa, and Ahmed Aly Sarhan. Electrical and optical properties of indium-tin oxide (ito) films by ion-assisted deposition (iad) at room temperature. *International Journal of Precision Engineering and Manufacturing*, 14(8):1465–1469, 2013.
- [S7] Farnood Khalilzadeh-Rezaie, Isaiah O. Oladeji, Justin W. Cleary, Nima Nader, Janardan Nath, Imen Rezadad, and Robert E. Peale. Fluorine-doped tin oxides for mid-infrared plasmonics. *Optical Materials Express*, 5(10):2184, 2015.
- [S8] Latifa Hanum Lalasari, Tri Arini, Lia Andriyah, F. Firdiyono, and Akhmad Herman Yuwono. Electrical, optical and structural properties of fto thin films fabricated by spray ultrasonic nebulizer technique from sncl4 precursor. *AIP Conference Proceedings*, May 2018.
- [S9] E. Shkondin, O. Takayama, M. E. Panah, P. Liu, P. V. Larsen, M. D. Mar, F. Jensen, and A. V. Lavrinenko. Large-scale high aspect ratio al-doped zno nanopillars arrays as anisotropic metamaterials. *Optical Materials Express*, 7(5):1606, 2017.
- [S10] Hong-lie Shen, Hui Zhang, Lin-feng Lu, Feng Jiang, and Chao Yang. Preparation and properties of azo thin films on different substrates. *Progress in Natural Science: Materials International*, 20:44–48, 2010.
- [S11] Zaka Ullah, Illani Nawi, Gunawan Witjaksono, Nelson Tansu, Muhammad Irfan Khattak, Muhammad Junaid, Muhammad Aadil Siddiqui, and Saeed Ahmed Magsi. Dynamic absorption enhancement and equivalent resonant circuit modeling of tunable graphene-metal hybrid antenna. *Sensors*, 20(11):3187, 2020.
- [S12] Hua Liu, Aparna Deshmukh, Nathan Salowitz, Jian Zhao, and Konstantin Sobolev. Resistivity signature of graphene-based fiber-reinforced composite subjected to mechanical loading. *Frontiers in Materials*, 9, 2022.